Physics of Plasmas

Sodium tracer measurements of an expanded dense aluminum plasma from e-beam isochoric heating

Cite as: Phys. Plasmas **28**, 033301 (2021); https://doi.org/10.1063/5.0040714
Submitted: 15 December 2020 . Accepted: 25 February 2021 . Published Online: 30 March 2021

N. B. Ramey, J. E. Coleman, P. Hakel, H. E. Morris, J. Colgan, J. E. Barefield, C. J. Fontes, R. M. Gilgenbach, and R. D. McBride

View Online Export Citation CrossMark

AIP Publishing Physics of Plasmas Features in Plasma Physics Webinars Register Today!

AIP Publishing

© 2021 Author(s).

Physics of Plasmas ARTICLE scitation.org/journal/php

Sodium tracer measurements of an expanded dense aluminum plasma from e-beam isochoric heating

Cite as: Phys. Plasmas **28**, 033301 (2021); doi: 10.1063/5.0040714
Submitted: 15 December 2020 · Accepted: 25 February 2021 ·
Published Online: 30 March 2021

View Online Export Citation CrossMark

N. B. Ramey,[1,2,a)] J. E. Coleman,[2] P. Hakel,[2] H. E. Morris,[2] J. Colgan,[2] J. E. Barefield,[2] C. J. Fontes,[2] R. M. Gilgenbach,[1] and R. D. McBride[1]

AFFILIATIONS

[1]University of Michigan, Ann Arbor, Michigan 48109, USA
[2]Los Alamos National Laboratory, Los Alamos, New Mexico 87545, USA

[a)]Author to whom correspondence should be addressed: nramey@lanl.gov

ABSTRACT

Spatially and temporally resolved visible absorption spectroscopy is performed on sodium D-lines present as surface contaminants on an expanded dense aluminum plasma plume. An 80-ns FWHM, intense, relativistic electron beam deposits 5.4 J into a 100-μm-thick Al foil, which isochorically heats and subsequently hydrodynamically expands the material through the warm dense matter state and into a classical-like plasma state, with a coupling parameter of approximately 0.2 and a degeneracy parameter of approximately 270. The Na contamination, carried along with the expanding plume, shows saturated absorption features in the dense Al continuum for $\lambda > 450$ nm. X-ray photoelectron spectroscopy and laser-induced breakdown spectroscopy confirm Na is a surface contaminant with an atomic concentration of ~0.1% when interrogating identical foil samples. A spectroscopic-quality radiation transport model is used to post-process 2D hydrodynamic simulations to interpret the plasma conditions based on the measured Na 3p-3s doublet line profiles. A sodium number density of 3×10^{15} cm^{-3} best matches the experimental spectra, which originate from a dense surface plasma with $n_e = 3.0 \pm 0.8 \times 10^{18}$ cm^{-3}.

Published under license by AIP Publishing. https://doi.org/10.1063/5.0040714

I. INTRODUCTION

Warm dense matter (WDM) is the region in phase space where the plasma is too dense ($0.1 < \rho_0 < 10$) to be described by ideal plasma theory and too warm ($0.1 < T_e < 10$ eV) to be described by condensed matter theory.[1,2] WDM has traditionally been investigated using high-powered laser systems[3] and pulsed power devices[4] as well as particle accelerators[5] and x-ray free electron lasers.[6] Recently, monochromatic electron beams are being used as an isochoric heating mechanism to produce large volumes of WDM.[7]

Electron beam-driven WDM production on an electron linac results in a strong Bremsstrahlung and scattered electron background, and diagnostics are being actively developed to perform measurements in the warm dense phase. The currently deployed diagnostics are in the visible regime and are measuring the plasma after it hydrodynamically expands into a dense, classical-like plasma with a coupling of $\Lambda = \frac{q_e^2}{4\pi\epsilon_0 k_B T_e}\sqrt[3]{\frac{4\pi n_e}{3}} \approx 0.2$ and a degeneracy of $\Theta = \frac{2m_e T_e}{\hbar^2 (3\pi^2 n_e)^{2/3}} \approx 270$.[8,9] Visible measurements are limited by opacity effects and, as such, only quantify the surface, rather than the bulk, plasma conditions. These measurements are thus sensitive to any spectroscopically significant contaminants that may be present on the foil surface, most notably sodium.

Laser-induced breakdown spectroscopy (LIBS) is used extensively to diagnose sample elemental composition and perform depth profiling with sensitivities down to 0.5% atomic concentration.[10] The plasma plume generated also permits evaluation of the self-absorption coefficient of resonance lines, which, in Al, include transitions belonging to Al–I and Al–II ions.[11–13] Sodium, in particular, is a contaminant readily found due to the strength of the 3p-3s doublet at 588.995 and 589.592 nm (historically known as the D-lines).[14–16] Sodium contamination can be introduced to samples through physical handling even with laboratory examination gloves (nitrile or latex) as measured by x-ray photoelectron spectroscopy (XPS).[17,18] XPS, sensitive to only the surface due to the range of the photoelectrons (8 nm in Al), complements LIBS as a diagnostic technique to quantify the elemental composition.

In this paper, we present measurements of sodium absorption lines (D-lines) present within the continuum generated by an

expanded dense aluminum plasma plume. The plasma is generated by focusing an intense, relativistic electron pulse with a kinetic energy of 19.8 MeV, a beam current of 1.45 kA, and a FWHM of 80 ns to a 1-mm-diameter spot on target.[19,20] The heating and hydrodynamic transitions from solid density, to dense plasma, and eventual classical plasma are shown in Fig. 1. The beam deposits a small fraction (5.4 J) of its total energy (2.3 kJ) into a range-thin 100-μm-thick Al foil. This low efficiency is due to the electron range (3.9 cm) being more than 300× the foil thickness. References 7–9 describe this process in detail. In short, the energy deposited, and thus the achievable plasma temperature, scales as $1/r_{beam}^2$, where r_{beam} is the electron beam radius at the foil surface. A spectroscopic-quality radiation transport model has been constructed to interpret the plasma conditions based on the intensities and ratio of the absorbed Na 3p-3s lines. XPS and LIBS analysis techniques are used to verify and quantify the sodium contaminants on the aluminum foils.

II. EXPERIMENTAL SETUP

These experiments are conducted using an electron beam to heat 100-μm-thick Al 1100 alloy foils.[21] As illustrated in Fig. 1, the energy deposited into the foil causes the material to heat, undergo phase transitions from the solid state to the plasma state, and expand hydrodynamically into the surrounding vacuum. The expanding plasma initially near solid density is opaque to visible light, which limits visible spectroscopy to later-time measurements, when the plasma begins to transition to lower densities.

Separate diagnostics are used to quantify the beam energy density, subsequent plasma plume expansion, and plasma characteristics: near-field optical transition radiation (OTR), plume visible self-emission imaging, and visible spectroscopy. The arrangement of these diagnostics is shown in Fig. 2.

Near-field OTR is used to measure the beam spot size at peak focus for energy density quantification. This is required for comparison with a hydrodynamics code, as described in Sec. III.

Visible plume self-emission imaging using a gated intensified CCD camera provides measurements of the plasma plume size.[8,9] A series of time-gated images yields a rough estimate of the plasma plume axial expansion velocity, subject to CCD sensitivity, dense plasma cutoff effects, and target paddle deflection in $\hat{z}$ (-300μm/in). A shadowgraphy and shearing interferometry system using a 70-mH, 532-nm, 5-ns laser is under development for future quantitative measurements of the plume expansion up to opacity limits.

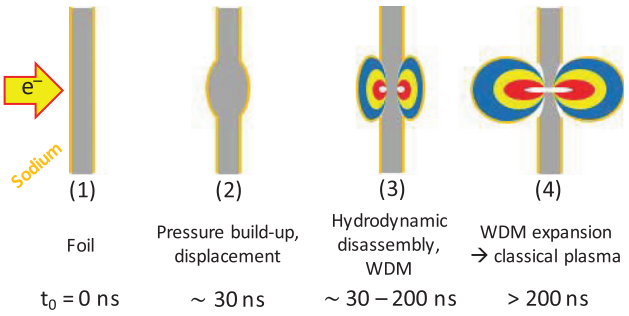

FIG. 1. Electron beam-driven WDM production. Approximate timescales are given for reference, where t_0 is the start of energy deposition. (1) The intense, relativistic electron beam is focused down to a small spot on the Al foil (gray) containing a surface contaminant (Na, orange). (2) Energy deposition results in a pressure build-up and displacement of the foil. (3) Hydrodynamic disassembly of the foil material and transition into the WDM stage. (4) Vacuum expansion of the WDM, which transitions later in time to a classical plasma. Spectroscopy measurements are presently being made temporally in and around (4).

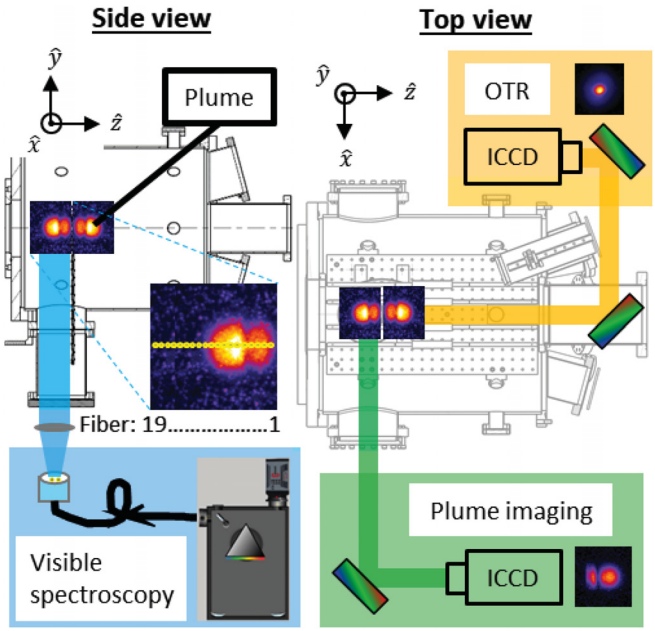

FIG. 2. Two views of the target diagnostic chamber configuration for visible absorption spectroscopy (blue), plume self-emission imaging (green), and near-field OTR imaging (orange). The target foil lies in the $\hat{x}$–$\hat{y}$ plane and the electron beam travels in the $\hat{z}$ direction. The OTR turning mirror sits 15° above the beam axis. Note that the coordinate system is left-handed.

Visible spectroscopy is performed on the upstream side of the target using a lens-coupled 19 × 200-μm-diameter linear fiber array oriented orthogonal to the foil surface (parallel to $\hat{z}$). A system magnification of 0.6 is achieved using a 180-mm focal length lens, resulting in a 7.68 mm axial coverage by the fiber array in the object plane. The 10-meter-long fiber bundle is fed into a 0.3-m focal length Czerny-Turner spectrometer (f/3.9) containing a triple-grating turret (150 G/mm, 500-nm blaze; 1800 G/mm, 500-nm blaze; 2400 G/mm, holographic).[22] Specific details on the spectrometer are provided in Ref. 23. All sensitive electronics (computers, CCDs, etc.) are staged approximately 8 feet away from the target diagnostic chamber to minimize potential radiation effects by the Bremsstrahlung produced during the electron beam pulse.

A. Measured spectra

The energy density throughout the duration of the beam is quantified with near-field OTR. Figure 3 shows a 5-ns gated image of the flat-top beam distribution on the aluminum target, 30 ns after the beginning of the beam pulse. The FWHM = 0.62 mm corresponds to a fluence of 190 kJ/cm^2. This results in isochoric heating of the solid foil until the pressure releases and the material begins to hydrodynamically disassemble.[7] The heated material is now a dense plasma and the

Published under license by AIP Publishing

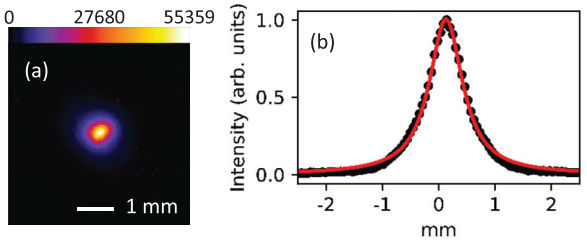

FIG. 3. Near-field OTR measurement on shot 28891. (a) Raw image with a color bar for the counts. (b) A Lorentzian fit of the spot shown in (a) provides a beam spot FWHM = 0.62 mm. The CCD resolution of the target is 54 μm/pixel.

electron beam continues to deposit energy into the expanding plasma plume.

Figure 4 details the plasma expansion using orthogonal visible self-emission plume imaging. The plume imaging shows cutoff effects from 50 to 150 ns likely due to the dense plasma that is opaque to visible photons. Plume ion expansion velocities and electron plasma temperatures are estimated by treating the plume as an ideal gas ($\gamma = 5/3$) expanding into a vacuum.[8,24] The leading-edge velocity is calculated using the FWHMs in Fig. 4(b), from which the electron temperature (T_e) is calculated using the relation $c_{s,ion} = \frac{\gamma-1}{2} v_{max} = \sqrt{\frac{\gamma k_B T_e}{m}}$, where m is the mass of the aluminum atom and $c_{s,ion}$ is the ion sound speed. We wish to emphasize that these v_{max} and T_e measurements are treated as rough order-of-magnitude estimations: we can say with certainty that the plasma plume has a $T_e \approx 1$ eV, based on previous measurements of other low-Z materials.[7–9] As previously mentioned, new diagnostics to more accurately assess plume extent (up to opacity limits) are actively being developed and will be used in lieu of this self-emission plume imaging diagnostic for future measurements.

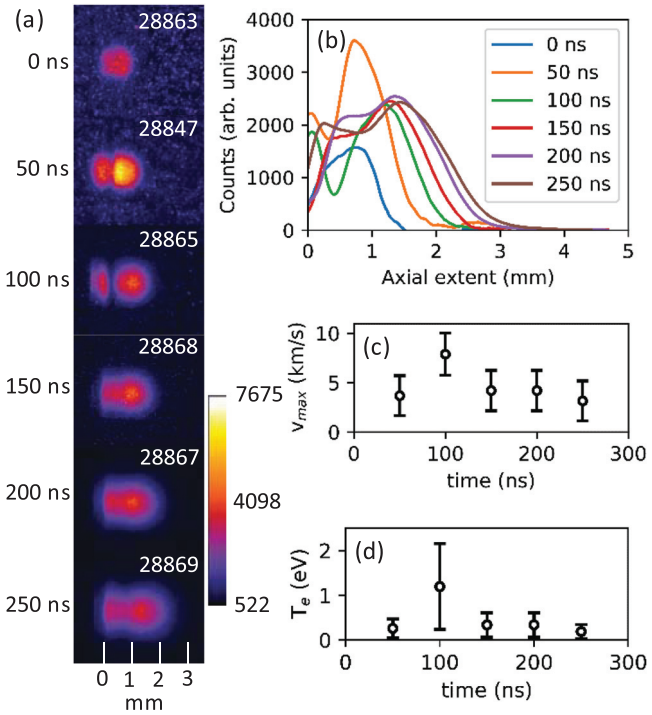

FIG. 4. Plume imaging sequence of shots showing plasma expansion and self-absorption. (a) The 50-ns gated image series beginning at $t_0 = 0$ ns. (b) The integrated axial intensities shown in (a). (c) The axial expansion velocity of the plume ions. By treating the expanding plume as an ideal gas, the temperature can be inferred and is shown in (d).

Three separate Al 1100 alloy foils were used as targets, with an average of seven shots per foil. Pilot desorption shots were first taken on each foil by defocusing the electron beam on the target face, which resulted in an incident fluence less than the melt phase transition. Subsequently, a spectral survey was performed and showed the presence of the Na D-lines absorbed on the Al continuum. Sodium absorption lines were clearly observed on 12 separate shots across the three different foils, confirming the reproducibility of the dataset.

A spectral survey of the plasma plume, shown in Fig. 5(a), shows strong continuum emission in the visible, perturbed by the Na D-lines at 590 nm. Figure 5(b) shows the absorbed D-lines beginning 200 ns after the start of energy deposition, where several fibers are clearly illuminated, with Fiber 6 and Fiber 10 located 2.1 ± 0.4 mm and 3.8 ± 0.4 mm upstream of the aluminum target face, respectively. The speckle present on the CCD for both Figs. 5(a) and 5(b) is likely due to charge deposited on the detector from the radiation background and is enhanced due to the increased gain. The increasing plasma density toward the foil surface results in decreased continuum levels measured (nearly 3× from Fiber 10 to Fiber 6), as shown in Fig. 5(c). The set of illuminated fibers is in reasonable agreement with the plume self-emission imaging data presented in Fig. 4(b), which has a FWHM of approximately 2.2 mm beginning 1 mm from the foil surface (note that fibers at axial distances ranging from 1.3–4.6 $\pm$ 0.4 mm have some level of continuum emission present).

Stark broadening is used to quantify the local surface plasma density using the absorbed Na 3p-3s doublet. Stark broadening is the dominant line broadening mechanism as the instrument width is < 0.20 nm and the Doppler width at 1 eV is 0.01 nm. In addition, the line profiles are not measurably Doppler shifted by the plasma motion. A total of six shots are fully analyzed to determine Stark widths as a function of axial distance from the foil surface. The following timeslices are referenced to the amount of time elapsed from the beginning of energy deposition; (t_0 + 100 ns) shots 28891 and 28894 illuminated Fibers 6–10, (t_0 + 200 ns) shots 28847, 28890, and 28895 illuminated Fibers 6–11, and (t_0 + 300 ns) shot 28889 illuminated Fibers 6–10. Stark widths of $w_m = 0.180$ and 0.185 Å/10^{17} cm^{-3} measured at a temperature of 15000 K are used for the 588.995 and 589.592 nm lines, respectively.[25,26] In Fig. 6, the data show that, as time increases, the surface plasma density generally evolves to lower densities. However, the trends of the two lines do not agree completely. Averaging $\langle n_e \rangle$ across all three timeslices gives $3.0 \pm 0.8 \times 10^{18}$ cm^{-3}. We are not claiming that this density constitutes the bulk plasma; it is only representative of the outermost layer of the plasma from which the measured photons are able to escape and reach the detector.

While the plasma is in local thermodynamic equilibrium (LTE),[27–29] the absorbed D-lines are saturated due to the large density from which they originate, meaning the expected optically thin line ratio of 2:1 given by the Einstein coefficients no longer holds true. This

Published under license by AIP Publishing

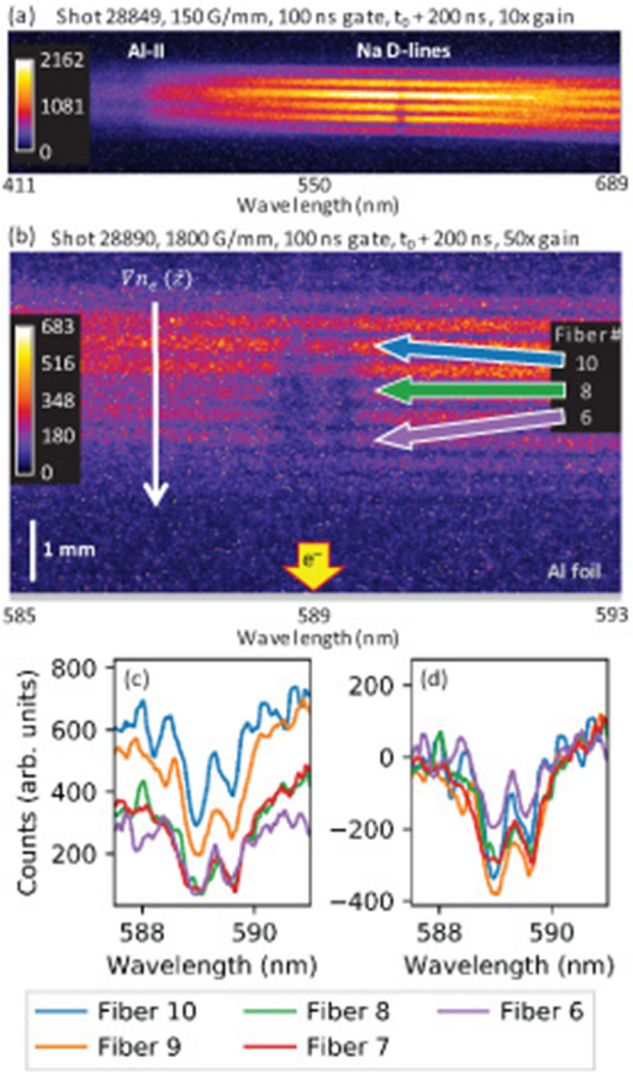

FIG. 5. Measured spectra: (a) low groove density, spectral survey establishing the continuum within which the Na D-lines are absorbed. (b) High groove density measurement focusing on the D-lines, both of which are clearly resolved. The time gate of both images is 200–300 ns after t_0. The aluminum foil surface and direction of the electron beam are also indicated. Lineouts of selected fibers indicate a significant variation in (c) the continuum intensity and (d) profiles of the absorbed D-lines. The peak line ratios for Fibers 6–10 are as follows: 1.17:1, 0.95:1, 1.06:1, 1.10:1, and 1.31:1.

behavior is exhibited by the spectra in Fig. 5 and will be further elaborated on in Sec. III B.

III. SPECTRAL MODELING

A simplified spectroscopic-quality radiation transport model has been created to interpret the experimental spectra observed in Fig. 5. The model integrates several codes to accomplish this task, including radiation-hydrodynamics (LASNEX[30]) radiation transfer (FESTR[31,32]) and the Los Alamos suite of atomic physics codes,[33] which includes atomic structure (CATS), ionization (GIPPER), and atomic kinetics

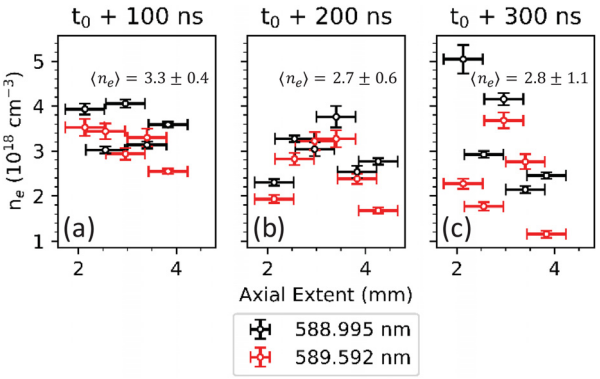

FIG. 6. Calculated electron densities (inferred from Stark widths for the 588.995 and 589.592 nm lines) across several well-illuminated fibers and three different timeslices. The densities in (a) and (c) decrease as the distance from the foil surface increases, while (b) shows a maximum around 3.5 mm. The spatially averaged electron density $\langle n_e \rangle$ trends to lower values at increasing times. The error bars shown for the inferred Stark electron densities are the standard errors from the Voigt fitting procedure. They do not include the 20% error bar from the documented Stark widths,[25,26] which are used to convert the FWHMs into electron densities.

(ATOMIC). Previous aluminum-only runs using SESAME EOS 3715[34] provided the basis for this model. While referred to as aluminum-only, they did in fact include a layer of water vapor on the foil surface, the presence of which is consistent with past experimental measurements.[35] An overview of how the LASNEX model is constructed is given in Ref. 7. For the analyses presented herein, we have found that it suffices to examine the individual axial slices immediately adjacent to the foil surface while hard-coding the sodium concentrations at each location. A full-scale 2D cylindrically symmetric hydrodynamic model of the plume expansion after heating by the electron beam, including the sodium presence, would be the most accurate approach; however, this is not trivial and will take a significant number of iterations to ensure correct material evolution. Such a model will be implemented in the near future.

A. Model description and physics

The aluminum-only radiation-hydrodynamics model is run in LASNEX to 400 ns with a 1-ns time step containing > 20 000 zones. The contents of these output files at each time step include the electron temperature, ion temperature, electron density, elemental number densities, total mass density, and velocity at each node. An IDL script is used to extract the desired axial locations at a given time slice from a hydro output file while interpolating the previously mentioned quantities along the radial extent.[36] This is required due to the evolution of the mesh as the simulation progresses in time.

Figure 7 illustrates the layout of the zones and detector used in FESTR, which employs a ray-trace method to sample the 2D structure of the LASNEX simulation to generate synthetic spectra. The sodium is placed in zones *i*, *j*, and *k* for axial slices located at Z_0, Z_1, and Z_2, respectively. The detector is built with patches located at each axial slice at a radius beyond the radial extent of the plume. We run FESTR with its tracking feature enabled, which records local spectra at the position of every zone and in the direction of the traversing ray. This approach allows for a detailed understanding of how the spectra

Published under license by AIP Publishing

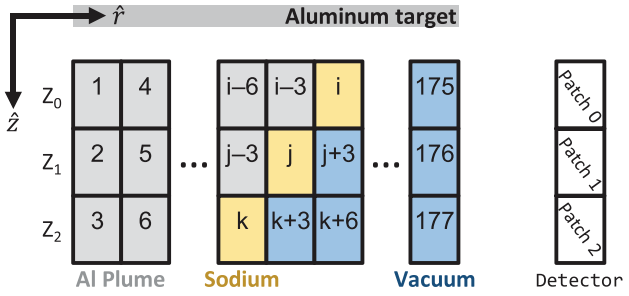

FIG. 7. Illustration (not to scale) of the truncated hydro geometry used in FESTR with the zones numbered as shown. The foil is centered at z = 0. The IDL routine extracts the desired chordal lineouts (Z_0, Z_1, and Z_2) from the full hydro output file. In this simplified model, the Na is placed at the outermost zone (maximum value of r) that contains aluminum, which borders the vacuum-containing zones. This distance is different for each lineout. The zones are revolved about the Z-axis to form toroids with quadrilateral cross sections. The detector is constructed with three patches, which correspond to the chordal lineouts.

observed for each chord are built up and what parts of the plasma contribute significantly to the final measured spectra.

Spectral databases are generated using the ATOMIC code for both sodium and aluminum over the relevant temperature range (0.25–1.5 eV; 0.05 eV steps) and electron density range (10^{15}–10^{21} cm^{-3}; ten points per decade) from the hydro model. Note that CATS calculates the level energies and transitions *ab initio*, so these values will not identically match the NIST tables,[37] but they are corrected by hand for experimental comparison. FESTR is then run to solve the radiation transport equation for photons as they pass through the simulated plasma plume. The current database is constructed by ATOMIC using no Stark broadening, so it is expected that the line widths produced by this model will not match experiment. However, the goal of this model is to match the line ratio and intensities, which are a direct function of the level populations that form the absorbed lines, in addition to any opacity effects that may impact the spectra formation. A good match of these quantities implies that the concentration of sodium atoms within the aluminum plasma plume is accurately captured.

B. Results and comparison with experimental measurements

The tracking capability of FESTR is displayed in Fig. 8, where we see how the spectra are formed as the ray passes from the far side (relative to the detector) to the near side of the plasma plume (transport from the top to the bottom of Fig. 8). At the outermost section of the plasma, the D-lines are observed in emission (blue trace, Fig. 8). When beginning to transit through the plasma, the lines are still being emitted but are superimposed on an increasing continuum due to the background aluminum plasma (orange trace, Fig. 8). Just before the ray exits the plasma, the continuum level is strong enough to dominate the D-line emissions (green trace, Fig. 8). Finally, once the ray escapes the plasma, the photons transit through the thin layer of sodium. The photons with energies corresponding to the D-line energies are absorbed, forming the final spectra observed by the detector (red trace, Fig. 8).

Figure 9 compares Fiber 10 from Fig. 5(c), located at an axial distance of 3.8 ± 0.4 mm from the foil surface, with four different sodium concentrations used in the radiation transport model. A sodium ion density of 3×10^{15} cm^{-3} shows the most reasonable agreement with the line intensities. However, a sodium ion density of 10^{16} cm^{-3} gives a line ratio of 1.36:1, which best matches the experimental line ratio of 1.31:1 with an error less than 4%. The line ratio, when further investigated using the radiation transport model, relaxes to the optically thin LTE ratio of 2:1 at sodium ion densities $\leq 10^{14}$ cm^{-3}. When the ion density is $\geq 5 \times 10^{16}$ cm^{-3}, the absorption lines are fully saturated, giving an effective ratio of 1:1. It is clear that the line profiles of the absorbed D-lines show a strong sensitivity to the concentration of sodium atoms present. The sensitivity of the line profiles will be further investigated in another study, along with attempting to observe the transition of spectral lines from absorption to emission due to the plume density gradients.

Calculated from the LASNEX results, the line-averaged ion density of the bulk aluminum plasma from 200 to 300 ns is 1.1×10^{21} cm^{-3} with an average ionization of $\bar{Z} = 0.48$. The temperature and density gradients seen at the given axial slice used to generate the synthetic spectra given in Fig. 9 remain relatively the same across the 100 ns window. In particular, the line-averaged electron (and ion) densities across three relevant timeslices (200, 250, and 300 ns) only vary by <10%, while the line-averaged electron temperatures are all within 3% of the time-averaged electron temperature of 0.37 eV. This demonstrates that the minimal error introduced by the time-integrated spectrometer measurement is negligible compared with uncertainties in the temperatures in Fig. 4(d) and electron densities in Fig. 6.

Note that the conditions of the bulk plasma satisfy the required conditions for LTE despite the Na D-line ratio not appearing in the expected optically thin LTE ratio of 2:1. This is a result of the large level populations of the ground state Na-I atom, which result in the resonant D-lines being optically thick. However, collisional processes still regulate the level populations, justifying the LTE approximation.[27–29] Based on the time-averaged $\langle n_e \rangle$ from Sec. II A and on the $\bar{Z}$ and best-fit n_{Na} from the model, we can infer locally the relative concentration of sodium atoms by dividing the sodium ion number density by the total ion number density. This yields an atomic concentration of 0.05 ± 0.02%.

IV. SODIUM CONTAMINATION QUANTIFICATION

After observing the Na lines experimentally from the electron energy deposition on the Al foils, we wish to understand the origin and amount of Na in the Al foil. XPS and LIBS are used as complementary measurements to quantify the location and amount of the Na contaminant. XPS uses a source of monoenergetic x rays incident upon the foil surface from which photoelectrons are emitted with energies characteristic of their originating atom's binding energy. By contrast, LIBS focuses a laser onto the foil surface, rapidly heating and ablating some of the material into a low-temperature plasma. This plasma acts as a source of emission lines from the atoms that makeup the plasma. These diagnostic tools yield elemental composition information from two fundamentally different processes. XPS will be sensitive to all elements that have electron binding energies less than the incident x-ray energy. LIBS is more limited in that the temperature (and density) of the plasma generated will determine the type of emission lines to escape the plasma and ultimately be detected.

A. LIBS measurements

LIBS is used to identify contaminants present on and within the aluminum foils. A 100-mJ, 8-ns Nd:YAG laser[38] operating at its

Published under license by AIP Publishing

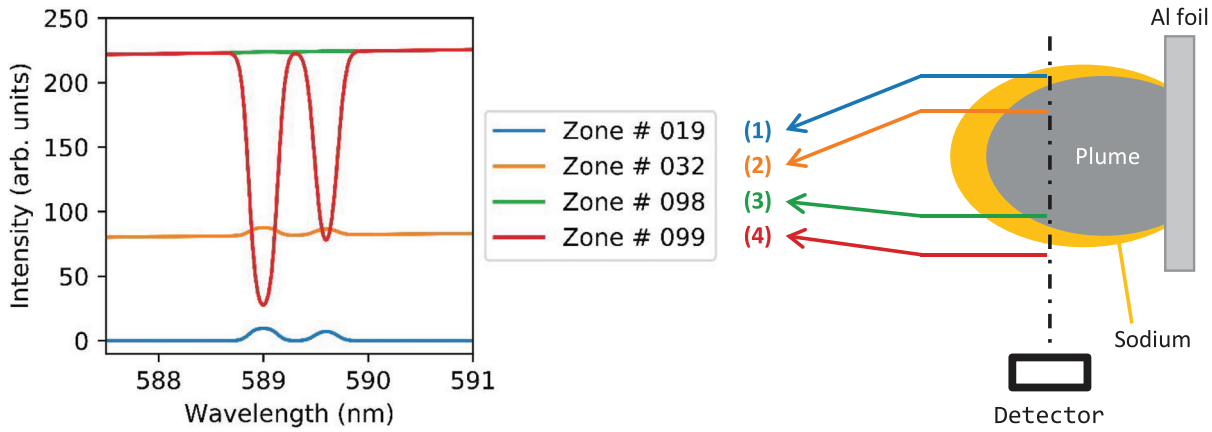

FIG. 8. Physical description of how the Na absorption lines ($n_{Na} = 10^{16}$ cm^{-3}) within the Al continuum are formed from the perspective of a photon traveling from top to bottom along the ray path (dash-dot line). (1) Optically thin emission of D-lines; (2) D-line emission on an increasing Al continuum; (3) dominant Al continuum all but covers D-line emission; (4) absorbed, saturated D-lines within a strong Al continuum. Note that these zone numbers are different than those shown in Fig. 7.

fundamental frequency and rep-rated at 5 Hz is focused onto the sample material in a 300-μm spot. The resulting energy deposition results in material ablation and heating to approximately 1 eV. This plasma is generally optically thin and produces emission lines characteristic of its constituents. An Echelle spectrograph is paired with a Raptor Photonics EMCCD to record the spectra over a wavelength range of 200–1000 nm.[39] The detector delay relative to the laser pulse is 1 μs, while the gate width is 5 μs. The experimental configuration is nearly identical to the second setup described in Sec. III of Ref. 28.

Three different foil samples (100-μm-thick, 99.999% pure Al;[40] 50-μm-thick Anodized Al;[41] and 100-μm-thick Al 1100 alloy[21]) were prepared for analysis using identical methods. The 1100 alloy was used for the electron beam heating experiments described in Sec. II A, while the others are used as comparison for sodium quantification. An ethyl alcohol wipe-down was performed using Kimwipes[42] while wearing nitrile gloves.[43] Care was taken to handle the foils only by the edges and to not touch them in the middle of the surface where the analysis would be performed. Each sample was wrapped in Kimwipes and placed within plastic cases for transport to the LIBS laboratory. In the LIBS laboratory, the cases were opened, and the samples were unwrapped and placed on the substrate mount using cleaned metal tweezers to carefully grasp only the corners of the foils.

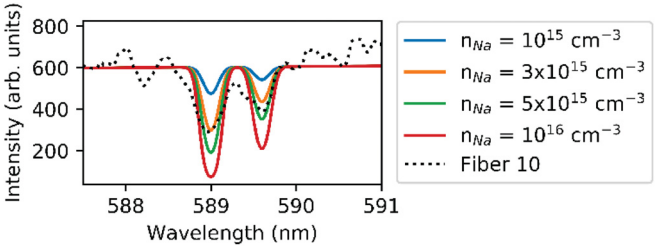

FIG. 9. Comparison of experimental results from Fig. 5(c) with the 1D radiation transport model. The most reasonable peak intensity comparison is obtained with a Na density of 3×10^{15} cm^{-3}. The line ratio calculated from the experimental data is 1.31:1. A density of 10^{16} cm^{-3} yields a simulated line ratio of 1.36:1, which best matches the measured line ratio.

The resulting spectra were analyzed after multiple groupings of 10 laser shots. Based on the laser parameters and the reflectivity of aluminum, it is estimated that each laser pulse bores approximately 800 nm into the material. By taking many tens of shots, an effective depth profile of the elements present can be determined. We expect to see the neutral aluminum lines corresponding to the 4s-3p doublet (394.401 nm and 396.152 nm) and 3d-3p triplet (308.215 nm, 309.271 nm, and 309.284 nm) to dominate the spectra. We also expect contributions from sodium (principally the strong D-lines, based on measurements in Figs. 5 and 9), in addition to other vacuum surface impurities like carbon, nitrogen, and oxygen. The lines are identified and matched to the measured spectra using the NIST Atomic Spectra Database.[37]

Figure 10 shows the results for two lines of interest: (a) Al–I 396.152 nm (4s-3p) and (b) Na–I 588.995 nm (3p-3s). The data were numerically integrated across the lines to investigate how the intensities varied as a function of depth into the material. As expected, across all three materials, the intensity of the Al line increases further into the sample. Although the trends are different, this behavior supports the argument that the bulk of the material is dominated by Al. This trend is followed by the other prominent Al–I lines at 394.401 nm, 308.215 nm, 309.271 nm, and 309.284 nm, with the only variation being in the relative amplitudes. Conversely, the Na D-line intensity decreases into the samples. Beyond 30 shots for the pure Al sample, the Na 588.995 nm line intensity was in the noise so no further data were collected, suggesting the Na contamination is limited to the surface for the pure Al foil. However, there is still significant D-line intensity observed well into the alloy and anodized Al foils, potentially indicating that the Na contamination could be both a surface and a bulk contaminant.

Figure 11 shows an overlay for the three different samples of the 4s-3p Al doublet (a.1–3), 3d-3p Al triplet (b.1–3), and the Na D-lines (c.1–3) from selected groupings of 10 shots corresponding to depths of approximately 0–8 μm, 8–16 μm, and 32–40 μm into the material, respectively. These spectra were background-subtracted before analysis to remove the Echelle grating artifacts at longer wavelengths as well as the Hg-I lines from ambient light. Note that in (b.1–3) the 309.271 nm

Published under license by AIP Publishing

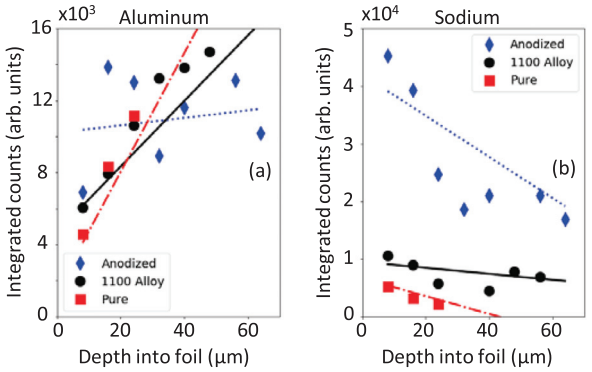

FIG. 10. LIBS results for the three different Al foils. Plotted are the integrated line intensities and linear regressions as a function of foil depth for (a) the Al–I 396.152 nm line and (b) the Na–I 588.995 nm line. The line intensity is proportional to the amount of that element which is present. The Al linear fits show, as a function of increasing foil depth, an increase in the Al presence. The Na data show that the pure foil only has Na contamination on the surface, while the alloy and anodized foils still have a significant amount of Na well within the bulk of the material. This behavior indicates that the pure foil is indeed chemically pure through the bulk, whereas the alloy and anodized foils have Na as both a surface and a bulk impurity.

and 309.284 nm lines are not resolved and appear as a single broad line. Further inspection of the Al–I lines shows that the plasma created by the LIBS laser varies from sample to sample; the anodized Al foil shows lines with larger wings than both the pure and alloyed Al samples. This could be due to the laser coupling more energy into the foil during the ablation process. This hypothesis is supported by the qualitative observation during the experiments that the popping sound produced by the shockwave of the expanding plume is louder for the anodized foil compared with the pure and alloy foils.

B. XPS measurements

XPS is used to provide a quantitative measurement of the surface contaminants present on the foils. The equipment used is a Kratos Axis Ultra XPS system located at the University of Michigan's Center for Materials Characterization.[44] This system has a sensitivity down to around one part per thousand or 0.1 at. %. An electron beam operating at 15 kV and 10 mA is accelerated onto an aluminum anode to produce characteristic K_α x rays. The x rays are then monochromated and focused onto the sample in a small ($<30\,\mu$m) spot, producing photoelectrons.

The electron emission occurs in a one- or two-step process. First, the x ray transfers its energy to an inner shell electron (1s, 2s, 2p, etc.) to create a core hole. This photoelectron is ejected from the atom in this one step process of photoionization. Subsequently, an outer-shell electron can fill the core-hole vacancy via radiative or Auger decay. In the latter process, another electron is ejected, subject to energy conservation, via the process of autoionization. Both the Auger electrons and photoelectrons are passed through a hemispherical analyzer that retards the electron energies and focuses them onto a detector. While the x rays may penetrate a few micrometers into the material, the electrons have a much shorter mean free path (λ_{mfp}) and only escape within roughly 3 λ_{mfp} of the surface. Therefore, the sampling depth for

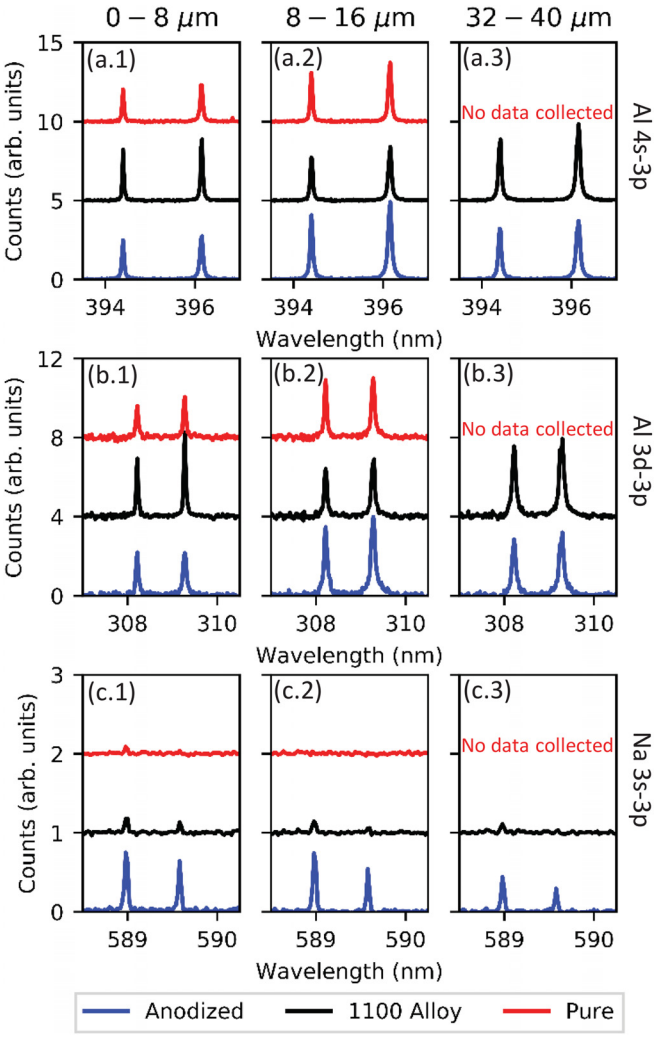

FIG. 11. Measured line profiles for the Al–I 4s-3p doublet (top row), Al–I 3d-3p triplet (middle row), and Na 3s-3p doublet (bottom row) at depths of 0–8 μm, 8–16 μm, and 32–40 μm. The lines for the three foils are vertically shifted to better show the differences between the intensities. All plots are identically scaled showing the Al–I lines are approximately 5× more intense than the Na–I lines, and the Al–I 4s-3p lines are slightly stronger than the Al–I 3d-3p lines. Note that the pure Al sample had shots taken no further than 16–24 μm deep so the third column presents data only for the anodized and alloy samples.

Al is limited to 8 nm, or 20 monolayers, so this is purely a surface interrogation technique.

The data collection was performed in survey mode over a bandwidth of 1200 eV to encompass the inner-shell and Auger peaks that could be produced by the various elements present on the sample surface. Figure 12 shows an example of the recorded spectra. Integrated peak counts are obtained by background-subtracting the continuum and then comparing these counts with the other peaks present. In this manner, XPS provides a quantitative measurement of the relative makeup of the material surface. All data processing was done using the CasaXPS software.[45]

Published under license by AIP Publishing

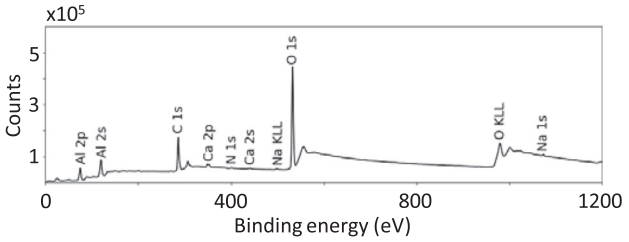

FIG. 12. Example XPS spectra (corresponding to case A in Table I). Here, all peaks that could significantly be observed in the spectra are highlighted. Only the strongest peaks from each species are used to calculate the at. % concentration shown in Table I.

XPS was performed on the Al 1100 alloy,[21] which was prepared in three different manners. Table I shows the results for the test cases with all data given in terms of at. %. Case A was minimally handled with Fisherbrand nitrile gloves[46] and wiped down using Kimwipes[42] and a 90% isopropyl alcohol solution. Case B was handled with slightly sweaty bare hands and subjected to no wipedown. Case C was liberally handled and touched all over with the same set of Fisherbrand nitrile gloves,[46] but no subsequent wipedown with isopropyl alcohol was performed.

The data clearly show, across all three cases, that aluminum, carbon, and oxygen dominate the elemental composition of the surface. However, there are also contributions from calcium, nitrogen, and sodium. Comparing case C to case A, when the foil was liberally handled with gloves and not wiped down, the carbon and calcium fractions increased along with a decrease in the aluminum and a slight decrease in the oxygen fractions. The sodium and nitrogen fractions cannot be said to have significantly changed due to the larger error bars associated with these measurements. Now, considering case B, where the foil was handled without gloves, the aluminum fraction dramatically decreases while the carbon fraction nearly doubles. Furthermore, the sodium fraction is now nearly 4× larger. These trends support that handling materials with bare hands will introduce a significantly higher amount of carbon and sodium contaminants on the surface of the aluminum. The calculated sodium atomic concentrations for case A and case C agree within the error bars with the inferred concentration from Sec. III B.

TABLE I. XPS results given for three different test cases on a 100-μm-thick Al 1100 alloy foil. Both cases A and C were investigated at two different locations on the same foil, and the data presented are the mean and 95% confidence interval for each. Case B is the result of a single experiment at a single location. All data are given in terms of the at. %. Note that a confidence interval of 0% is an artifact of having only two data points.

Element	Case A (at. %)	Case B (at.%)	Case C (at. %)
C 1s	42±10%	83%	66±5%
O 1s	31±5%	12%	19±2%
Al 2p	25±6%	34%	13±3%
Ca 2p	1.0±0.0%	0.23%	1.5±0.3%
N 1s	0.43±0.26%	0.77%	0.28±0.00%
Na 1s	0.095±0.069%	0.39%	0.075±0.010%

C. Comparison of results

The largest discrepancy between the XPS and LIBS results are the carbon lines. Carbon dominates the XPS spectra while it is virtually unobserved in the LIBS data. This is most likely due to the difference in the way each technique probes and then measures the samples. XPS can detect almost any element because there will always be some bound electron of that element that can be ejected and then detected. Conversely, LIBS spectra are determined by the plasma produced and the sensitivity of the spectrometer and detector. The majority of carbon's strong and prominent lines according to the NIST tables[37] lie < 200 nm, and the detector used for the LIBS setup is only sensitive to wavelengths > 200 nm, so it is likely that carbon lines are being produced given the plasma conditions, but the detector is simply not sensitive to them. The same argument holds true for the oxygen lines.

Nonetheless, both diagnostic techniques confirm the presence of sodium contamination. XPS initially demonstrated a measurable concentration of sodium atoms on the surface on the order of a few parts per thousand, but this small amount was not conclusive due to the diagnostic limitations. However, the LIBS results corroborate the XPS results by clearly measuring the spectral signature of the sodium D-lines.

V. CONCLUSION

Sodium absorption lines have been observed on an expanding dense aluminum plasma plume heated by an intense, relativistic, monochromatic electron beam. The contamination location and amount was quantified using two fundamentally different techniques, XPS and LIBS. The sodium was determined primarily to be a surface contaminant across pure, anodized, and 1100 alloy aluminum, consisting of about 10 monolayers. This conclusion is supported by a decrease in the line intensity of the sodium D-lines when boring into the sample using LIBS. However, the alloy and anodized foils have a significant Na presence within the foils, suggesting that Na is an impurity embedded within the material lattices, while the pure Al foil is indeed chemically pure.

These results motivated the construction of a spectroscopic-quality radiation transport model to interpret the plasma conditions using the profiles of the absorbed D-lines. The model shows an acute sensitivity to the sodium ion concentration with the best intensity match at $n_{Na} = 3 \times 10^{15}$ cm^{-3} and best line ratio match at $n_{Na} = 10^{16}$ cm^{-3}. The unsaturated line ratio of 2:1 of the resonant Na D-lines requires $n_{Na} < 10^{14}$ cm^{-3}. Stark broadening analysis of the experimental absorption spectra from the plasma plume gives an average electron density of $3.0 \pm 0.8 \times 10^{18}$ cm^{-3}. This, combined with the measured line ratios near 1:1, suggests that the saturated absorption lines originate from a dense, highly collisional outer layer of the plasma plume. The inferred sodium atomic concentration from both the simplified radiation transport model and the Stark broadening measurements agrees with the XPS results from case A and case C, which justifies the use of the basic radiation transport model. Further experiments will be performed to improve and refine the modeling capability, including validation of the hydrodynamics model with time-resolved visible interferometry. They will also attempt to observe the transition of spectral lines from absorption to emission.

Published under license by AIP Publishing

ACKNOWLEDGMENTS

This work was supported by the U.S. Department of Energy through the Los Alamos National Laboratory. Los Alamos National Laboratory is operated by Triad National Security, LLC, for the National Nuclear Security Administration of U.S. Department of Energy (Contract No. 89233218CNA000001). The authors acknowledge the financial support of the University of Michigan College of Engineering and NSF grant #DMR-0420785 and technical support from the Michigan Center for Materials Characterization for the XPS experiments. The authors would like to thank the anonymous referees for their careful review of this manuscript and for their helpful suggestions.

DATA AVAILABILITY

The data that support the findings of this study are available from the corresponding author upon reasonable request.

REFERENCES

[1]Committee on High Energy Density Plasma Physics, National Research Council, *Frontiers in High Energy Density Physics: The X-Games of Contemporary Science* (The National Academies Press, Washington, DC, 2003).
[2]R. W. Lee, S. J. Moon, H. K. Chung, W. Rozmus, H. A. Baldis, G. Gregori, R. C. Cauble, O. L. Landen, J. S. Wark, A. Ng, and S. J. Rose, J. Opt. Soc. Am. B **20**, 770 (2003).
[3]M. Koenig, A. Benuzzi-Mounaix, A. Ravasio, T. Vinci, N. Ozaki, S. Lepape, D. Batani, G. Huser, T. Hall, and D. Hicks, Plasma Phys. Controlled Fusion **47**, B441 (2005).
[4]R. E. Reinovsky, in *IEEE Pulsed Power Conference* (IEEE, Washington, DC, 2009), pp. 203–208.
[5]P. A. Ni, M. I. Kulish, V. Mintsev, D. N. Nikolaev, V. Ya. Ternovoi, D. H. H. Hoffmann, S. Udrea, A. Hug, N. A. Tahir, and D. Varentsov, Laser Part. Beams **26**, 583 (2008).
[6]R. W. Lee, H. A. Baldis, R. C. Cauble, O. L. Landen, J. S. Wark, A. Ng, S. J. Rose, C. Lewis, D. Riley, J.-C. Gauthier, and P. Audebert, Laser Part. Beams **20**, 527 (2002).
[7]J. E. Coleman, H. E. Morris, M. S. Jakulewicz, H. L. Andrews, and M. E. Briggs, Phys. Rev. E **98**, 043201 (2018).
[8]J. E. Coleman and J. Colgan, Phys. Rev. E **96**, 013208 (2017).
[9]J. E. Coleman and J. Colgan, Phys. Plasmas **24**, 083302 (2017).
[10]M. Sabsabi and P. Cielo, Appl. Spectrosc. **49**, 4 (1995).
[11]F. Colao, V. Lazic, R. Fantoni, and S. Pershin, Spectrochim. Acta, Part B **57**, 1167 (2002).
[12]A. M. El Sherbini, T. M. El Sherbini, H. Hegazy, G. Cristoforetti, S. Legnaioli, V. Palleschi, L. Pardini, A. Salvetti, and E. Tognoni, Spectrochim. Acta, Part B **60**, 1573 (2005).
[13]Q. L. Ma, V. Motto-Ros, W. Q. Lei, M. Boueri, X. S. Bai, L. J. Zheng, H. P. Zeng, and J. Yu, Spectrochim. Acta, Part B **65**, 896 (2010).
[14]J. A. J. M. Van Vliet and J. J. De Groot, IEE Proc. A **128**(6), 415 (1981).
[15]J. J. De Groot and J. A. J. M. Van Vliet, *The High-Pressure Sodium Lamp*, 1st ed. (Macmillan Education, UK, 1986), pp. 15–27.
[16]J. P. Woerdman and J. J. De Groot, ACS Symp. Ser. **179**, 33 (1982).
[17]A. Plasencia, J. D. Piasecki, and B. R. Strohmeier, Spectroscopy **27**(7) (2012), available at https://www.spectroscopyonline.com/view/xps-surface-characterization-disposable-laboratory-gloves-and-transfer-glove-components-other-surfac.
[18]K. Archuleta, presented at the 61st Annual Technical Meeting and Exposition of IEST, Danvers, MA, 2015, SAND2015-2366C.
[19]J. E. Coleman, D. C. Moir, C. A. Ekdahl, J. B. Johnson, B. T. McCuistian, G. W. Sullivan, and M. T. Crawford, Phys. Rev. ST Accel. Beams **17**, 030101 (2014).
[20]J. E. Coleman, C. A. Ekdahl, D. C. Moir, G. W. Sullivan, and M. T. Crawford, Phys. Rev. ST Accel. Beams **17**, 092802 (2014).
[21]See https://www.mcmaster.com/foils/aluminum/easy-to-form-pure-1100-aluminum-sheets-and-bars-7/ for Al alloy foils.
[22]See https://www.princetoninstruments.com/learn/calculators/grating-dispersion for "Grating Dispersion Calculator."
[23]J. E. Coleman, Rev. Sci. Instrum. **87**, 123113 (2016).
[24]P. L. G. Ventzek, Ph.D. thesis, University of Michigan, Ann Arbor, 1991.
[25]J. Purić, J. Labat, S. Djenize, L. Cirković, and I. Lakićević, Phys. Lett. **56A**, 83 (1976).
[26]J. F. Baur and J. Cooper, J. Quant. Spectrosc. Radiat. Tarnsfer **17**, 311 (1977).
[27]R. W. P. McWhirter, *Plasma Diagnostic Techniques* (Academic Press, New York, 1965).
[28]J. Colgan, E. J. Judge, D. P. Kilcrease, and J. E. Barefield, Spectrochim. Acta, Part B **97**, 65 (2014).
[29]H. R. Griem, J. Quant. Spectrosc. Radiat. Transfer **8**, 389 (1968).
[30]G. B. Zimmerman and W. L. Kruer, Comments Plasma Phys. Controlled Fusion **2**, 51 (1975).
[31]P. Hakel, Comput. Phys. Commun. **207**, 415 (2016).
[32]See https://github.com/LANLhakel/FESTR for the current version of the FESTR code.
[33]C. J. Fontes, H. L. Zhang, J. Abdallah, Jr., R. E. H. Clark, D. P. Kilcrease, J. Colgan, R. T. Cunningham, P. Hakel, N. H. Magee, and M. E. Sherrill, J. Phys. B **48**, 144014 (2015).
[34]SESAME Library, Report No. UCID-118574-82-2 (Lawrence Livermore National Laboratory, 1982).
[35]C. Vermare, H. A. Davis, D. C. Moir, and T. P. Hughes, Phys. Plasmas **10**, 277 (2003).
[36]H. E. Morris, private communications (April 2020).
[37]A. Kramida, Y. Ralchenko, and J. Reader, *NIST ASD Team 2014 NIST Atomic Spectra Database v. 5.2* (NIST, Gaithersburg, MD, 2014); See https://www.nist.gov/pml/atomic-spectra-database for documented lines and levels.
[38]See https://www.quantel-laser.com/en/products/item/ultra-50-100-mj–134.htm for the Quantel Laser.
[39]See http://www.catalinasci.com/emu.cfm for EMU-65 UV/VIS/NIR Spectrograph and EMCCD.
[40]See http://www.goodfellow.com/E/Aluminium-Foil.html for pure Al foils (AL000565).
[41]See https://www.filmtools.com/blacstudfoil-5954.html and https://www.thorlabs.us/thorproduct.cfm?partnumber=BKF12 for anodized Al foils.
[42]See https://www.kcprofessional.com/en-us/products/wipers/specialty-wipers/34155 for Kimwipes.
[43]See https://www.ansell.com/us/en/products/touchntuff-92-600 for TouchNTuff® Gloves (NBR 92-600, lot 1503411905).
[44]See https://mc2.engin.umich.edu/techniques/kratos-axis-ultra-xps/ for "Kratos Axis Ultra XPS."
[45]See http://www.casaxps.com/ for CasaXPS Software.
[46]See https://www.fishersci.com/shop/products/fisherbrand-powder-free-nitrile-exam-gloves-24/p-2826798 for Fisherbrand Gloves (Re-order # 19-130-1597D and 19-041-171D).

Published under license by AIP Publishing